



# Solar-blind UV photodetectors based on $\alpha$ -Ga<sub>2</sub>O<sub>3</sub> prepared by a two-step hydrothermal method

Junjun Xue<sup>1</sup> · Kaicheng Xu<sup>1</sup> · Jiaming Tong<sup>1</sup> · Zhouyu Chen<sup>2</sup> · Haoyu Fang<sup>2</sup> · Saisai Wang<sup>3</sup> · Jin Wang<sup>1</sup> · Ting Zhi<sup>1</sup>

Received: 7 April 2024 / Accepted: 7 June 2024 / Published online: 26 June 2024

© The Author(s), under exclusive licence to Springer Science+Business Media, LLC, part of Springer Nature 2024

## Abstract

In this study,  $\alpha$ -Ga<sub>2</sub>O<sub>3</sub> nanorod arrays (NRAs) were grown using a simple and low-cost two-step hydrothermal method. Subsequently, a photoelectrochemical ultraviolet photodetector (PEC-UV PD) based on the  $\alpha$ -Ga<sub>2</sub>O<sub>3</sub> NRAs was fabricated, which can operate at zero bias and has a performance far superior to that of PEC-UV PDs based on the one-step hydrothermal method. Under 2 mW/cm<sup>2</sup> illumination at 254 nm, the device achieved a responsivity of 26.59 mA/W, an external quantum efficiency of 12.98%, and a rise/decay time of 53 ms/7 ms without external bias. These results demonstrate outstanding detection performance compared to previously reported devices. The superior performance can be attributed to the better crystallinity which provides a larger absorption area for the device, the solution contact area, and a faster channel for carrier transport, the space charge region at the solid/liquid interface which also allows efficient separation of photogenerated carriers. Furthermore, it also benefits from the positive effects of moderate oxygen vacancy (V<sub>O</sub>) concentrations for NRAs. The  $\alpha$ -Ga<sub>2</sub>O<sub>3</sub> NRAs PEC-UV PD with two-step hydrothermal method is undoubtedly a promising candidate for future solar-blind detection.

**Keywords**  $\alpha$ -Ga<sub>2</sub>O<sub>3</sub> · Hydrothermal · PEC photodetector · Self-powered · Solar-blind

✉ Saisai Wang  
sswang@smail.nju.edu.cn

✉ Jin Wang  
jin@njupt.edu.cn

✉ Ting Zhi  
zhit@njupt.edu.cn

<sup>1</sup> College of Electronic and Optical Engineering and College of Flexible Electronics (Future Technology), Nanjing University of Posts and Telecommunications, Nanjing 210023, China

<sup>2</sup> Portland Institute, Nanjing University of Posts and Telecommunications, Nanjing 210023, China

<sup>3</sup> School of Electronic Science and Engineering, Nanjing University, Nanjing 210023, China

## 1 Introduction

The solar spectrum can usually be divided into the visible, infrared, and ultraviolet bands (Hu et al. 2011, 2014; Chen et al. 2021; Guo et al. 2023; He et al. 2023). Within ultraviolet (UV) light, it can be meticulously divided into long-wave UV (UVA, low frequency, 400–315 nm), medium-wave UV (UVB, medium frequency, 315–280 nm), and short-wave UV (UVC, high frequency, 280–200 nm) according to the wavelength of the light (Pearton et al. 2018). UVC radiation from the sun is reflected and absorbed by ozone, water vapor, and other atmospheric molecules in the atmosphere, making it scarcely detectable at the surface of the Earth. Consequently, this wavelength range is often referred to as solar-blind UV. As it is not affected by the background noise of the sunlight, there are a wide range of potential applications for solar-blind light detection, such as biomedicine, UV monitoring, UV communications, solar-blind imaging, and missile tracking (Wu et al. 2017, 2021; Ahn et al. 2021; Wang et al. 2020a; Zhuo et al. 2018; Mahmoud 2016).

In recent years, many attempts have been made to construct UV photodetectors from suitable materials (Guo et al. 2023). At this stage, wide-bandgap materials commonly used for the preparation of solar-blind UV photodetectors include AlGa<sub>x</sub>N, MgZnO, Ga<sub>2</sub>O<sub>3</sub>, and diamond (Tsao et al. 2017; Cicek et al. 2013; Hou et al. 2013; Kong et al. 2016; Liao et al. 2010). The bandgap of diamond is 5.5 eV, which is very inefficient for the solar-blind band (Gorokhov et al. 2011), while the bandgaps of silicon carbide (SiC, 3.3 eV) (Morkoç et al. 1994) and gallium nitride (GaN, 3.4 eV) (Lan 2021) are sufficient for the near-ultraviolet band but are no longer suitable for the solar blind band below 280 nm. In addition, the Al<sub>x</sub>Ga<sub>1-x</sub>N material can be adjusted by the Al component to meet solar-blind detection. However, when the Al content is too heavy, a large number of defects appear in the thin film (Chi et al. 2022). Similarly, MgZnO undergoes severe phase separation as the proportion of Mg elements rises, which ultimately leads to a reduction in device performance. Ga<sub>2</sub>O<sub>3</sub>, a new wide-bandgap semiconductor material, is a natural deep ultraviolet probe material due to its bandgap between 4.4 and 5.3 eV (Akaiwa and Fujita 2012; Onuma et al. 2015; Fujita et al. 2016) and its response peak in the solar-blind band (Orita et al. 2000; Chen et al. 2016).

However, most current Ga<sub>2</sub>O<sub>3</sub>-based photodetectors are the metal–semiconductor–metal (MSM) type and need to be supported by an external power supply, which limits their use in a variety of extreme conditions. The Ga<sub>2</sub>O<sub>3</sub>-based electrochemical self-powered solar-blind photodetector has a promising future because it does not require an external power supply and has low manufacturing costs. Recently, Zhang et al. (2022a) have grown and fabricated  $\alpha$ -Ga<sub>2</sub>O<sub>3</sub> NRAs PEC PDs on FTO substrates by a one-step hydrothermal method, and the devices are capable of self-powered operation with a responsiveness of 3.87 mA under solar blind light illumination only. Zhang et al. (2018) and Atilgan et al. (2020) have successfully grown  $\beta$ -Ga<sub>2</sub>O<sub>3</sub> nanowires with superior crystal morphology on Si substrates using a two-step hydrothermal method. They added anhydrous ethanol to the reaction solution during the first hydrothermal step, which eased the surface tension between the solution and the substrate, allowing more nucleation sites to appear on the substrate. The central idea of the method is to use solution effects to alter the interaction of solution clusters with the surface.

In this work, the  $\alpha$ -Ga<sub>2</sub>O<sub>3</sub> NRAs were synthesized on FTO glass substrates via a two-step hydrothermal method and fabricated the  $\alpha$ -Ga<sub>2</sub>O<sub>3</sub> NRAs PEC-UV PD. Compared to other reported Ga<sub>2</sub>O<sub>3</sub>-based UV photodetectors, the  $\alpha$ -Ga<sub>2</sub>O<sub>3</sub> NRAs PEC-UV PDs

exhibited higher responsiveness, higher external quantum efficiency, and faster responsivity rates.

## 2 Experimental details

### 2.1 Synthesis and characterization of the $\alpha$ -Ga<sub>2</sub>O<sub>3</sub> NRAs

Firstly, the FTO substrate was cleaned with acetone, alcohol, and deionized water (DIW) to remove impurities from the substrate surface. Secondly, the reaction solution for the two hydrothermal steps was prepared separately: the solution for the first hydrothermal step consisted of 10 ml anhydrous ethanol (99.5%), 30 ml DIW and 0.3 g gallium nitrate (Ga(NO<sub>3</sub>)<sub>3</sub>) solution (Ga 9–10% w/w, Alfa Aesar Co., Ltd); the solution for the second hydrothermal step consisted of 30 ml DIW and 0.3 g Ga(NO<sub>3</sub>)<sub>3</sub> solution. Both hydrothermal solutions were stirred at room temperature for about 30 min to allow the components to mix thoroughly. The FTO substrate and the solution for the first hydrothermal step were then transferred to a stainless-steel reactor lined with PTFE, heated at 100 °C for 1 h, and allowed to cool naturally to room temperature. The reaction solution was then replaced with the second hydrothermal solution and heated at 150 °C for 10 h. Afterwards, the FTO glass with the GaOOH precursors was repeatedly rinsed with alcohol, DIW and dried in a desiccator at 70 °C for 2 h. Finally, the completely dried samples were placed in a muffle furnace set at 400 °C and annealed in air for 4 h to obtain  $\alpha$ -Ga<sub>2</sub>O<sub>3</sub> NRAs. We have labeled this two-step hydrothermal growth sample as Sample II. For a valid comparison, we have grown a similar sample using only the second hydrothermal step (30 ml DIW and 0.3 g Ga(NO<sub>3</sub>)<sub>3</sub> solution), noted as Sample I, according to previous reports (Zhang et al. 2022a). Figure 1 shows the schematic diagrams of one-step hydrothermal and two-step hydrothermal synthesis of  $\alpha$ -Ga<sub>2</sub>O<sub>3</sub> NRAs. It is worth noting that there is a short nucleation phase during the crystal growth process, which is usually overlooked and will be discussed below. We subjected the one-step samples (Sample I) to an 11-h hydrothermal reaction as well as a 4-h annealing to ensure that both samples experienced consistent thermal reaction times.

To determine the morphological characteristics and material composition of the two samples, simple scanning electron microscope (SEM) and X-ray diffraction (XRD) characterization tests were carried out. The crystalline phase and structure of the samples were

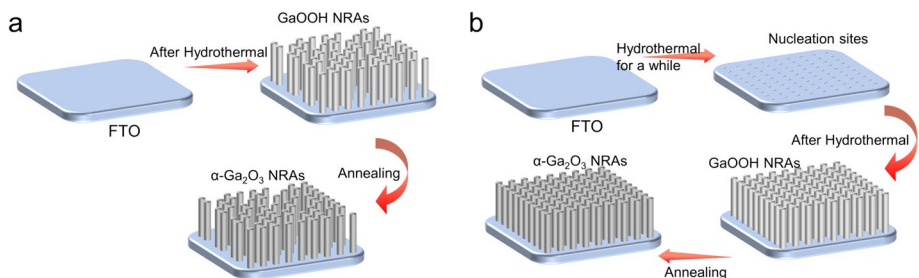


**Fig. 1** **a** Schematic diagram of the one-step hydrothermal synthesis of  $\alpha$ -Ga<sub>2</sub>O<sub>3</sub> NRAs (Samples I). **b** Schematic diagram of the two-step hydrothermal synthesis of  $\alpha$ -Ga<sub>2</sub>O<sub>3</sub> NRAs (Sample II)

characterized using the XRD (Bruker AXS, D8 Advance) emitting Cu  $K_{\alpha}$  radiation. SEM was used to observe the microstructure of the samples.

## 2.2 Fabrication of the electrochemical ultraviolet photodetector (PEC-UV PD)

The fabricated solar-blind photodetectors were tested for photovoltaic properties, etc., using a CHI 760E electrochemical workstation (CH Instruments, Chenhua Co., Shanghai). In the PEC setup, FTO glasses grown with  $\alpha$ -Ga<sub>2</sub>O<sub>3</sub> NRAs are held in place by platinum electrode clamps as photoanodes, with a platinum mesh electrode ( $1 \times 1$  cm<sup>2</sup>) and a saturated calomel electrode (SCE) as counter electrodes. The reaction solution for PEC was 0.5 M Na<sub>2</sub>SO<sub>4</sub> aqueous solution. LED beads with wavelengths of 254 nm, 265 nm, 275 nm, 295 nm, 310 nm, and 365 nm were used as the UV light source. The effective light area of the device is approximately 1 cm<sup>2</sup>.

## 3 Results and discussion

The top SEM views of Sample I and Sample II are shown in Fig. 2a, b, respectively. In Sample I which has not experienced the first hydrothermal step, there are more incompletely grown nanorods (as shown in the circles in Fig. 2a). While in Sample II which has undergone two hydrothermal steps, there are only very few incompletely grown nanorods, most of which show approximately the same edge length (~240 nm). It can be clearly observed that the nanorods in Sample I are mostly tilted at an angle to the substrate, whereas the nanorods in Sample II grow almost perpendicular to the substrate. Figure 2c,

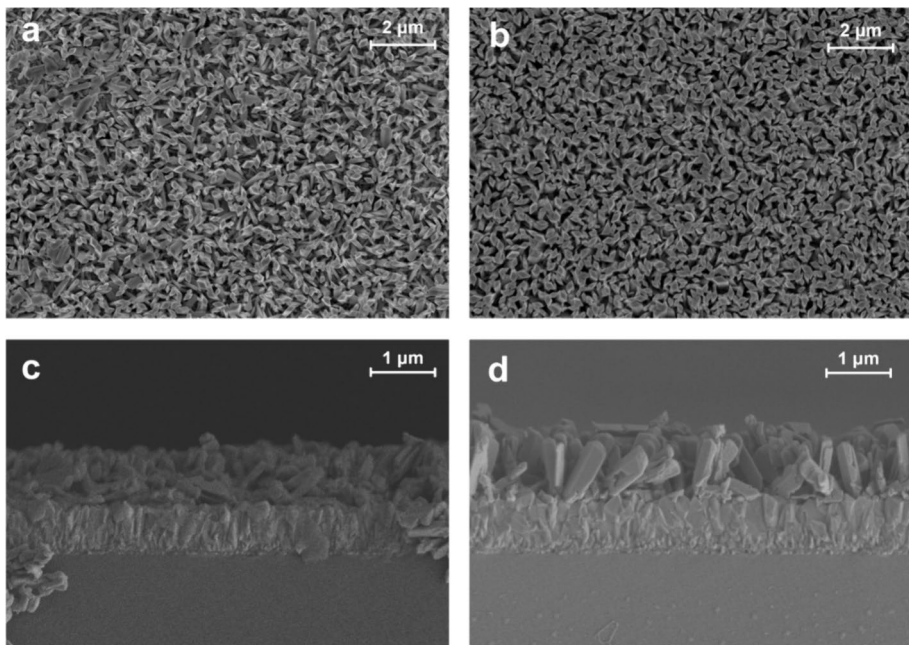


**Fig. 2** a SEM top view of Sample I and b Sample II. c SEM side view of Sample I and d Sample II

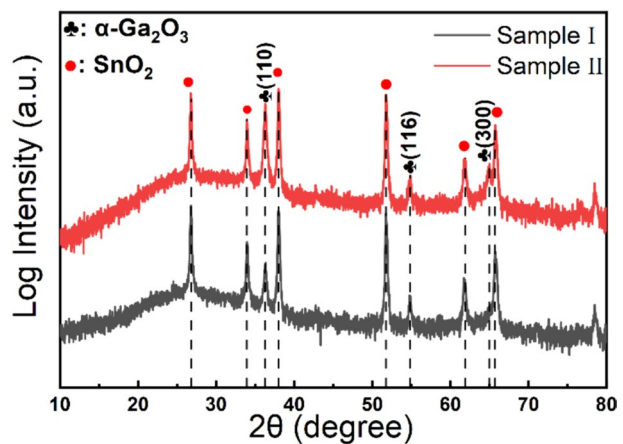
d shows a side view of both samples, and it is clear that Sample II has a larger size and a more complete crystal morphology.

Figure 3 shows the XRD plots. The  $2\theta$  angles at  $36.025^\circ$ ,  $55.114^\circ$ , and  $64.777^\circ$  correspond to the (110), (116) and (300) planes of  $\alpha$ -Ga<sub>2</sub>O<sub>3</sub> (PDF#06-0503) respectively. The remaining spurious peaks all originate from the SnO<sub>2</sub> component of the FTO substrate, indicating that the sample contains no other impurities, ensuring satisfactory crystal growth. Furthermore, we can clearly observe that Sample II has a much higher peak level in the (110) plane than Sample I, indicating that the two-step hydrothermal method is more suggesting more directional rods towards (110) plane.

According to classical crystal growth theory (Fujihara et al. 2005; Lewis 1974), crystal growth in solution is usually divided into two basic steps: The first step is called the nucleation phase, where the solute is transported from the solution to the solution/substrate interface due to the gradient in solute concentration at the substrate and solution interface, and then adheres to the substrate to form a nucleus. The second step, known as the crystal growth phase, becomes the driving force for crystal growth due to the great difference in concentration gradients brought about by the nucleation phase in the previous step (Fujihara et al. 2005), which allows the crystal to start growing based on the nucleation sites. In general, the density of nucleation sites is proportional to the concentration of the solution, with higher precursor concentrations giving more nucleation sites to the substrate (Liang et al. 2017). When we consider the hydrophobicity of the hydrothermal solution (Ga<sup>3+</sup>/H<sub>2</sub>O) and the FTO surface, the Ga<sup>3+</sup> ions are not readily adsorbed by the FTO substrate, so even with a higher concentration of solution it fails to bring about more nucleation sites, and the nanorods grow in clusters around these limited sites. At this point, several or even more nanorods grow on a nucleation site, and there is also competition between these nanopillars. According to Oswald's ripening theory (Reddy et al. 2015), the Gibbs free energy of the small particles is larger than that of the large particles, resulting in a higher concentration of parent phase components around the small particles than the large particles, and the concentration gradient creates diffusion, which in turn results in the small particles continuously delivering supersaturated components to the large particles, with the final nanorod exhibiting a high shape size difference.

According to the theory of R.W. Thomas with the hypernetted-chain approximation (Chan et al. 1978; Li et al. 2015), the solute distribution on the hydrophobic surface

**Fig. 3** XRD plots of Sample I and Sample II



depends on the contact angle between the solution and the substrate (Li et al. 2015), and when ethanol is added to the solvent, the adhesion of the mixed solution is improved at this point, thus changing the contact angle between the solution and the substrate (Kokkoli et al. 1999). As shown in Fig. S1 (Supporting Information), we applied drops of DIW and an ethanol/DIW mixture to the FTO glass, respectively, and the ethanol-treated solution lay completely flat on the substrate. Because of the addition of ethanol, the surface tension of water is reduced, making it easier for the  $\text{Ga}^{3+}$  ions to adhere to the FTO substrate, thus increasing the nucleation site density. During the subsequent crystal growth process, more nucleation sites eased the competition for the nanopillars, which were eventually grown uniformly to form  $\alpha\text{-Ga}_2\text{O}_3$  NRAs with good morphology and excellent crystallinity.

We have tested the photovoltaic properties of  $\alpha\text{-Ga}_2\text{O}_3$  NRAs PEC-UV PDs in a quartz cell containing a  $\text{Na}_2\text{SO}_4$  reaction solution in conjunction with an electrochemical workstation. The optical responsivity characteristics were first tested on two samples at  $2\text{ mW/cm}^2$ , 254 nm wavelength illumination, and 0 V bias voltage at 10 s On/Off intervals. As shown in Fig. 4a, the photocurrent density of Sample I is approximately  $24.052\ \mu\text{A/cm}^2$ , while the photocurrent density of Sample II is approximately  $51.08\ \mu\text{A/cm}^2$ . The Sample II exhibits a higher photocurrent density, due to the higher number of nucleation sites from the first hydrothermal step which guarantees a high crystallinity and a favorable array structure of the crystal. Larger cross-sectional areas and longer nanorod heights allow for a larger surface area for UV light absorption and easier device generation of photogenerated carriers. Similarly, this increases the contact area between the device and the electrolyte, and photogenerated carriers are more easily transferred from the  $\alpha\text{-Ga}_2\text{O}_3$  NRAs into the electrolyte (Lin et al. 2016; Chen et al. 2019; He et al. 2019).

In addition, to investigate the ability of the device to detect solar-blind light signals, we measured the photocurrent and the corresponding responsiveness under different wavelengths of UV illumination, as shown in Figs. 4b and S2 (Supporting Information). Both samples showed the largest photocurrent density at 254 nm and the highest responsivity (Sample I: 12 mA/W, Sample II: 26.59 mA/W). As the wavelength moves closer to the near-UV band, the photocurrent density as well as the responsiveness of the device decreases. Sample II achieved a photocurrent rejection ratio ( $I_{254\text{ nm}}/I_{365\text{ nm}}$ ) of  $1.274 \times 10^5$  in the solar blind band (254 nm) and the near ultraviolet band (365 nm), indicating that the  $\alpha\text{-Ga}_2\text{O}_3$  NRAs can detect the solar blind signal well without interference from other wavelengths of ultraviolet light. This is assisted by the ultra-wide bandgap of  $\alpha\text{-Ga}_2\text{O}_3$ , which makes it extremely sensitive to solar blind signals without any energy band engineering. The UV-vis spectroscopy of the two samples is shown in Fig. S3 (Supporting Information).

Subsequently, the focus was on the light detection performance of  $\alpha\text{-Ga}_2\text{O}_3$  NRAs PEC-UV PDs under solar blind illumination (254 nm). The linear scanning voltammetry (LSV) characteristic curves of  $\alpha\text{-Ga}_2\text{O}_3$  NRAs PEC-UV PDs in the dark and under 254 nm light are shown in Figs. S4 and S5 (Supporting Information). The very weak dark currents exhibited by both samples at 0 V as well as the pronounced photocurrents demonstrate the self-powered capability of the  $\alpha\text{-Ga}_2\text{O}_3$  NRAs PEC-UV PD. The I-t curves of the  $\alpha\text{-Ga}_2\text{O}_3$  NRAs (Sample II) PEC-UV PD at 0 V,  $0.5\text{--}2\text{ mW/cm}^2$  optical power are shown in Fig. 4c. The results show that the prepared detector can respond immediately and produce a relatively stable photocurrent at the Off/On transition, indicating that the device has achieved good sensitivity and stability. The effect of light intensity on PD performance is further discussed to visualize the relationship between optical power and photocurrent. Figure 4d shows the photocurrent density generated by the device at different light intensities. When the light intensity is gradually increased from  $0.5$  to  $2\text{ mW/cm}^2$ , the photocurrent density

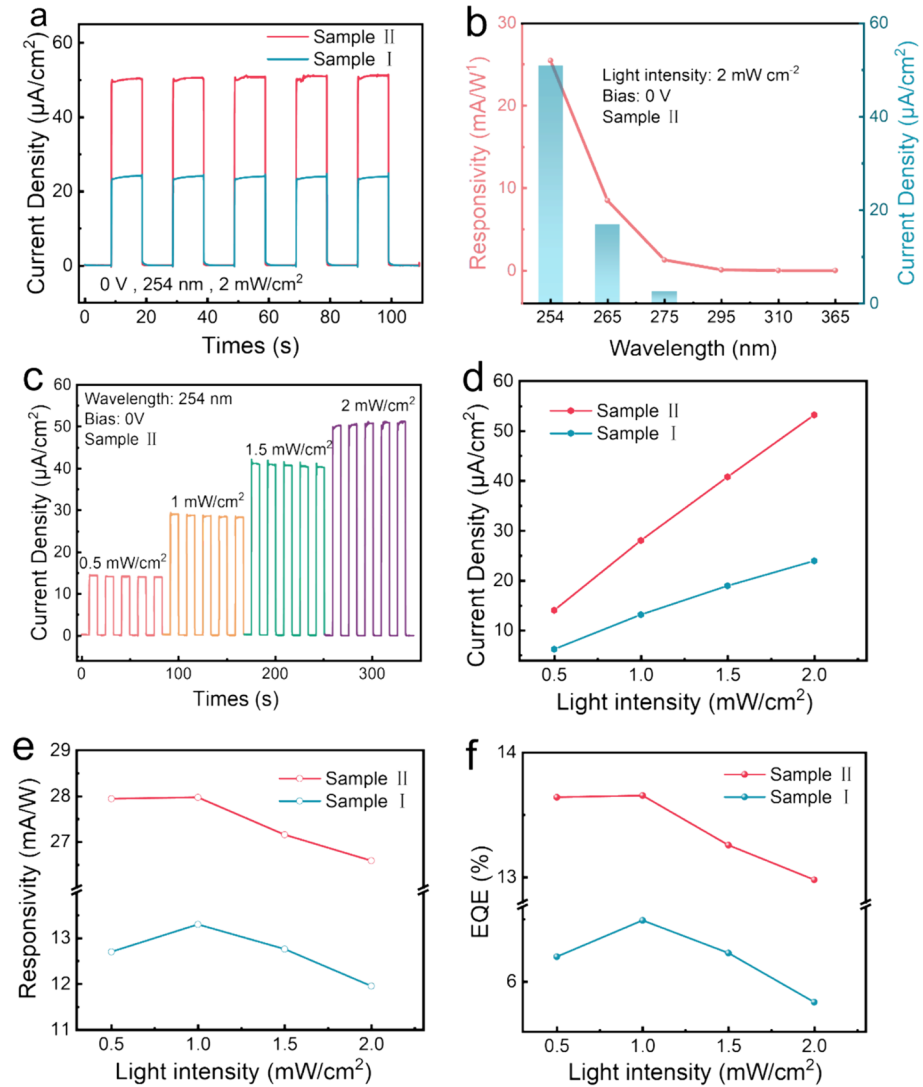


**Fig. 4** **a** I-t curves of Sample I and II under 0 V bias voltage and 2 mW/cm<sup>2</sup>, 254 nm UV illumination. **b** Spectral responsivity patterns of Sample II under different wavelengths of UV illumination and the corresponding photocurrent density. **c** I-t curve of  $\alpha$ -Ga<sub>2</sub>O<sub>3</sub> NRAs (Sample II) PEC-UV PD under different light intensity irradiation at 0 V. **d** Relationship between photocurrent and light intensity. **e** Plot of responsiveness versus light intensity. **f** Plot of efficiency versus light intensity

increases from 14.176  $\mu\text{A}/\text{cm}^2$  to 51.08  $\mu\text{A}/\text{cm}^2$ , indicating that higher light intensity can stimulate more photogenerated electron–hole pairs, thus generating a larger photocurrent. In addition, the dark current density of the device at a light intensity of 2 mW/cm<sup>2</sup> is merely 0.0289  $\mu\text{A}/\text{cm}^2$ , with a light-to-dark current ratio ( $I_{\text{photo}}/I_{\text{dark}}$ ) of 1767.

We usually measure the performance of a photodetector in terms of responsivity (R) and external quantum efficiency (EQE). Responsiveness is defined as  $R = (I_{\text{photo}} - I_{\text{dark}}) / (S \cdot P)$ .

where  $I_{\text{photo}}$  is the photocurrent,  $I_{\text{dark}}$  is the dark current,  $S$  is the effective light area and  $P$  is the light intensity (Li et al. 2019). The external quantum efficiency is usually defined as  $\text{EQE} = (Rhc)/e\lambda$ , where  $R$  is the responsivity,  $h$  is Planck's constant,  $c$  is the speed of light,  $e$  is the electron charge and  $\lambda$  is the wavelength of incident light (Zhang et al. 2019a). The responsivity curves and EQE curves for the two samples are shown in Fig. 4e, f. Under UV illumination at 254 nm, 2 mW/cm<sup>2</sup>, and 0 V, the responsivity and EQE of the Sample II were 26.59 mA/W and 12.98%, respectively. As the optical power increases, both  $R$  and EQE show a slight decrease, which we speculate may be due to the fact that higher light intensities excite more photogenerated carriers, but also increase the compounding of electron–hole in the nanorods, and the proportion of photogenerated carriers that can be used effectively decreases (Li et al. 2019; You et al. 2019; Yan et al. 2020). However, we found that the responsivity curves of Sample I did not follow a regular monotonic decrease, probably due to the sequence of tests and the fact that UV illumination changed the surface wettability.  $\alpha\text{-Ga}_2\text{O}_3$  NRAs converted from hydrophobic to hydrophilic would be more susceptible to redox reactions with  $\text{Na}_2\text{SO}_4$  solutions, enhancing the photoresponsivity.

When irradiated with UV light (254 nm) at photon energies higher than the band gap of  $\alpha\text{-Ga}_2\text{O}_3$ , electrons ( $e^-$ ) in the valence band will be excited to the conduction band, while the same number of holes ( $h^+$ ) will be generated in the valence band. Some of these holes will react with lattice oxygen to form surface oxygen vacancies ( $V_{\text{O}}$ ) and some of the electrons will react with lattice metal ions  $\text{Ga}^{3+}$  to form  $\text{Ga}^{2+}$  defects. Water and oxygen in solution will compete to dissociate and adsorb at these sites.  $\text{Ga}^{2+}$  tends to react with surface oxygen molecules, while at the same time water molecules will be coordinated to the  $V_{\text{O}}$ , causing the dissociative adsorption of water. Thus, the wettability of  $\alpha\text{-Ga}_2\text{O}_3$  has changed from hydrophobic to hydrophilic. However, the time required for this hydrophilic transition varies in different nanomorphology. The shorter the hydrophilic transition time for nanostructures with larger contact areas, as reported by Khranovskyy et al. (2012). The order of increasing light intensity was used in our responsiveness tests. Therefore, we presume that the transition to wettability was completed at the time of the 0.5 mW/cm<sup>2</sup> light intensity test when testing the Sample II because of the larger surface area. For Sample I, however, due to its smaller surface area, it took longer to generate sufficient water dissociation adsorption sites, so it only converted to hydrophilic at 1 mW/cm<sup>2</sup> light intensity tested. This resulted in a higher responsivity for Sample I at 1 mW/cm<sup>2</sup> than at 0.5 mW/cm<sup>2</sup>.

In addition to the effect of light intensity, the optical responsivity performance of the device is also affected by the applied bias voltage. Figure 5a shows the photocurrent density of the  $\alpha\text{-Ga}_2\text{O}_3$  NRAs (Sample II) PEC-UV PD at different bias voltages. As the bias voltage rises, the photocurrent generated by the device also follows. This is because the applied bias voltage accelerates the drift of the photogenerated carriers and increases the probability of separation of the electron–hole pairs (Ahmadi et al. 2017), so the device will be more responsive at higher bias voltages. To further evaluate the optical responsivity speed of the device, the rise time and decay time of the Samples I and II are shown in Fig. 5c,d. The rise time ( $\tau_r$ ) is defined as the time it takes for the photocurrent density to rise from 10 to 90% of its maximum value, and the decay time ( $\tau_d$ ) is the time used for the photocurrent density to fall from 90 to 10% of the maximum value. The rise time/decay time is 53 ms/7 ms for Sample II and 84 ms/9 ms for Sample I, with a particularly significant rise time improvement (31 ms). This enhancement is brought about by the high quality of the crystals. Longer and wider nanorods allow for more contact with the electrolyte solution and more light absorption area, while better crystallinity provides a faster channel for carrier transport, thus increasing the response times. In addition, we performed stability tests on the device for up to 1000 s (~50 cycles), as shown in Figs. 5b and S6 (Supporting



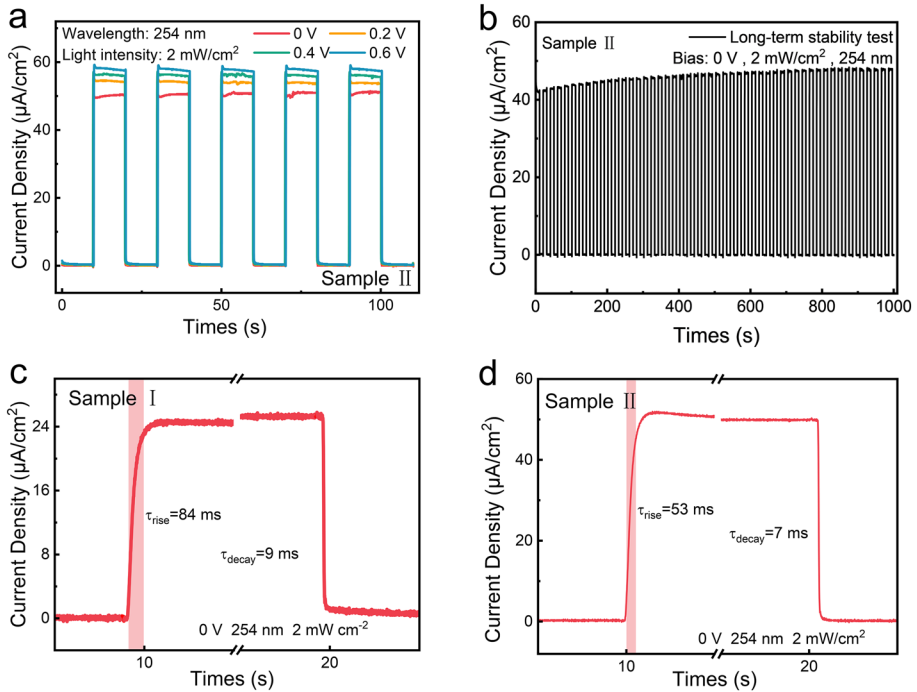


**Fig. 5** **a** Photocurrent responsivity of  $\alpha$ -Ga<sub>2</sub>O<sub>3</sub> NRAs (Sample II) PEC-UV PD at 0 V, 0.2 V, 0.4 V and 0.6 V under 254 nm, 2 mW/cm<sup>2</sup> illumination. **b** Long-term stability test image of  $\alpha$ -Ga<sub>2</sub>O<sub>3</sub> NRAs (Sample II) PEC-UV PD under zero bias and 254 nm, 2 mW/cm<sup>2</sup> illumination. **c** Rise time and decay time of Sample I. **d** Rise time and decay time of Sample II

Information). After 50 on/off cycles, the photocurrent density of the device remained at a promising level, indicating that the UV photodetectors have a good stability.

To investigate in depth the self-powered characteristics and operating mechanism of the  $\alpha$ -Ga<sub>2</sub>O<sub>3</sub> NRAs PEC-UV PD, we have drawn a schematic diagram as shown in Fig. 6.

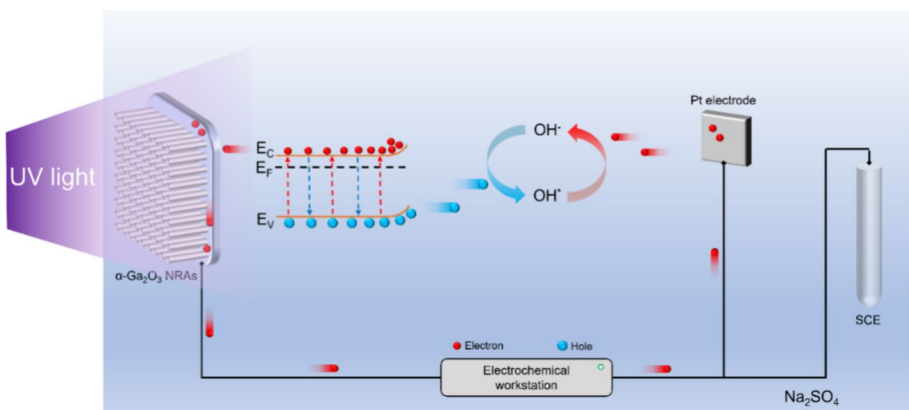


**Fig. 6** Schematic diagram of the mechanism of  $\alpha$ -Ga<sub>2</sub>O<sub>3</sub> NRAs PEC-UV PD

When  $\alpha\text{-Ga}_2\text{O}_3$  NRAs are in contact with  $\text{Na}_2\text{SO}_4$  electrolyte solution, the Fermi energy level ( $E_F$ ) of  $\alpha\text{-Ga}_2\text{O}_3$  is greater than the redox potential ( $E_{O/R}$ ) of  $\text{Na}_2\text{SO}_4$  (He et al. 2019). To bring the Fermi energy level and redox potential back into dynamic equilibrium, electrons within the semiconductor are transferred to the electrolyte solution, which causes an upward bending of the energy band on the semiconductor surface and the creation of a space charge region (with a built-in electric field pointing from  $\alpha\text{-Ga}_2\text{O}_3$  to the  $\text{Na}_2\text{SO}_4$  solution) (Wang et al. 2022). When the  $\alpha\text{-Ga}_2\text{O}_3$  NRAs are irradiated by UV light, photogenerated electron–hole pairs are produced and they are separated by the built-in electric field. The photogenerated electrons are separated and transferred to the Pt electrode via the conductive layer on the surface of the FTO substrate and the external circuit and undergo a reduction reaction with  $\text{OH}^*$  in solution ( $e^- + \text{OH}^* \rightarrow \text{OH}^-$ ). And photogenerated holes are driven to the solid/liquid interface to undergo oxidation with  $\text{OH}^-$  ( $h^+ + \text{OH}^- \rightarrow \text{OH}^*$ ) (Zhang et al. 2021; Bai and Zhang 2016; Li et al. 2013). As long as they are exposed to a constant stream of UV light, the photogenerated electron–hole pairs can be driven by the built-in electric field to continuously separate and react with the solution in a continuous redox reaction, thus achieving a self-powered effect. The reason for the better performance of Sample II is that there are enough nucleation sites in the crystal growth phase to allow the nanorods to be well formed.

In photodetectors based on  $\text{Ga}_2\text{O}_3$  thin films, methods such as high oxygen annealing and oxygen plasma treatment are often used to reduce the oxygen vacancy ( $V_O$ ) concentration in the material (Zhang et al. 2022b; Wang et al. 2020b; Guo et al. 2014). This is because  $V_O$  is generally thought to create trap states on the surface, leading to severe surface compounding and a reduction in photocurrent (Guo et al. 2014). In fact, the presence of  $V_O$  during PEC increases the carrier concentration (when  $V_O$  is generated in a semiconductor, the extra electrons compensate for the charge, leading to a boost in n-type semiconductor carrier concentration), enhances charge transfer, and inhibits in body complexation (Wang et al. 2019a). Therefore, a reasonable  $V_O$  concentration is of extreme benefit for the performance enhancement of  $\alpha\text{-Ga}_2\text{O}_3$  NRAs PEC-UV PDs. As shown in Fig. 7a, we fitted the equivalent series resistance ( $R_s$ ) and the interfacial charge transfer resistance ( $R_{ct}$ ) of two  $\alpha\text{-Ga}_2\text{O}_3$  NRAs PEC-UV PDs by electrochemical impedance spectra (EIS).  $R_s$  is positively proportional to  $V_O$  concentration and  $R_{ct}$  is inversely proportional to  $V_O$

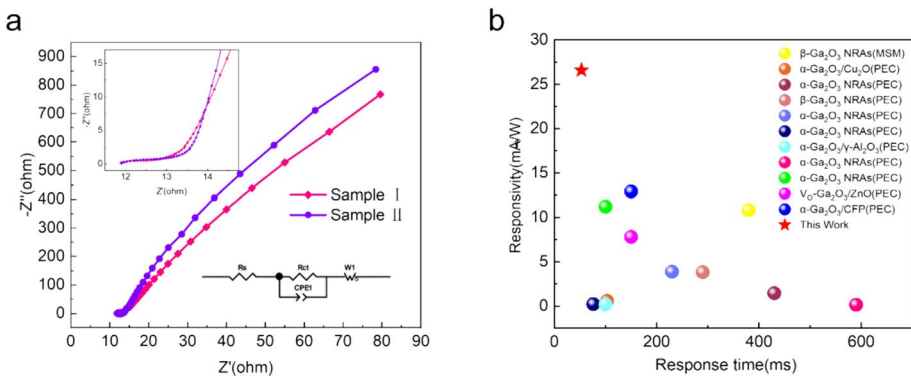


**Fig. 7** **a** The measured electrochemical impedance spectra (EIS) of Samples I and II. Inset: Enlarged view of EIS and Analog circuit diagrams. **b** Comparison of the responsivity speed and responsivity of previously reported  $\text{Ga}_2\text{O}_3$ -based UV photodetectors with this work

concentration. The smaller the  $R_s$ , the faster the photogenerated carrier transport, and the smaller the  $R_{ct}$ , the faster the interfacial charge transfer, resulting in greater photocurrents (Qu et al. 2023). The  $R_s$  and  $R_{ct}$  of our fitted Sample II are: 11.5  $\Omega$  and 9,994  $\Omega$ , while the two resistance values of Sample I are: 11.31  $\Omega$  and 117  $\Omega$ , respectively. After upgrading from the one-step to the two-step method,  $\Delta R_s$  is 0.19  $\Omega$  and  $\Delta R_{ct}$  is -107.006  $\Omega$ . The trend of  $R_{ct}$  is greater than  $R_s$ , so the optical responsivity in our  $\alpha$ -Ga<sub>2</sub>O<sub>3</sub> PEC-UV PDs is mainly modulated by  $R_{ct}$ . Since the Sample II has a smaller  $R_{ct}$ , it has a higher  $V_O$  concentration and the surface will attract more OH<sup>-</sup> ions for reaction, accelerating the charge transfer at the interface and bringing a higher photoresponsivity.

As shown in Fig. 7b, we have compared this work with other work on Ga<sub>2</sub>O<sub>3</sub>-based photodetectors (Zhang et al. 2022a, 2021, 2019b; Chen et al. 2019; He et al. 2019; Wang et al. 2023, 2019b; Ni et al. 2022; Huang et al. 2021a, b). Our  $\alpha$ -Ga<sub>2</sub>O<sub>3</sub> NRAs PEC-UV PD exhibits higher responsiveness and faster response times than other Ga<sub>2</sub>O<sub>3</sub>-based PEC PDs. In addition, other performance parameters are comparable to or better than those previously reported. The advantages of the device are: (i) the preparation of  $\alpha$ -Ga<sub>2</sub>O<sub>3</sub> NRAs using a very low-cost hydrothermal method, (ii) better UV absorption and fast separation of carriers due to the larger surface area and excellent crystallinity of the NRAs, (iii) appropriate concentrations of  $V_O$  increase the n-type carrier concentration and accelerate the interfacial charge transfer.

## 4 Conclusions

In this study, we have fabricated an  $\alpha$ -Ga<sub>2</sub>O<sub>3</sub> NRAs PEC-UV PD based on a two-step hydrothermal method. The built-in electric field formed at the solid/liquid interface allows the device to operate without an applied voltage and to exhibit favorable optoelectronic properties. In particular, the optical responsivity reached 26.59 mA/W,  $I_{photo}/I_{dark}$  reached 1767 and the rise and decay times of the optical responsivity were 53 ms and 7 ms at 254 nm, 2 mW/cm<sup>2</sup>, and zero bias. The excellent crystallinity, fast separation of photogenerated carriers, and better transport channels are responsible for the superior performance. Furthermore, the proper use of  $V_O$  also accelerates the interfacial charge transfer for the device. These results demonstrate that the  $\alpha$ -Ga<sub>2</sub>O<sub>3</sub> NRAs PEC-UV PD, fabricated using the two-step hydrothermal method, emerges as a highly promising candidate for future solar-blind detection applications.

**Supplementary Information** The online version contains supplementary material available at <https://doi.org/10.1007/s11082-024-07174-0>.

**Acknowledgements** This work was funded by the National Key R&D Program of China (Grant No. 2022YFB3605403), the National Natural Science Foundation of China (Grant Nos. 62374094, 62104110, 61974062, 62004104), the Natural Science Foundation of Jiangsu Province (Grant Nos. BK20200094, BK20210577), the Project funded by China Postdoctoral Science Foundation (2023T160332), the open research fund of the National and Local Joint Engineering Laboratory of RF Integration and Micro-Assembly Technology.

**Author contributions** Junjun Xue: Conceptualization, Data curation, Supervision, Writing-original draft, Writing-review & editing; Kaicheng Xu: Conceptualization, Methodology, Data curation, Writing-original draft; Jiaming Tong: Investigation, Validation, Visualization, Formal analysis; Zhouyu Chen: Investigation, Data curation, Validation; Haoyu Fang: Investigation, Validation, Formal analysis; Saisai Wang: Data curation, Validation, Visualization, Writing-review & editing; Jin Wang: Conceptualization, Methodology, Supervision, Writing-review & editing; Ting Zhi: Investigation, Methodology, Supervision, Writing-review & editing;

**Data availability** The datasets generated during and/or analyzed during the current study are available from the corresponding author on reasonable request.

## Declarations

**Competing interests** The authors declare no competing interests.

## References

- Ahmadi, M., Wu, T., Hu, B.: A review on organic-inorganic halide perovskite photodetectors: device engineering and fundamental physics. *Adv. Mater.* (2017). <https://doi.org/10.1002/adma.201605242>
- Ahn, J., Ma, J., Lee, D.: Ultrahigh deep-ultraviolet responsivity of a  $\beta$ -Ga<sub>2</sub>O<sub>3</sub>/MgO heterostructure-based phototransistor. *ACS Photon.* **8**(2), 557–566 (2021). <https://doi.org/10.1021/acsp Photonics.0c01579>
- Akaiwa, K., Fujita, S.: Electrical conductive corundum-structured  $\alpha$ -Ga<sub>2</sub>O<sub>3</sub> thin films on sapphire with tin-doping grown by spray-assisted mist chemical vapor deposition. *Jpn. J. Appl. Phys.* (2012). <https://doi.org/10.1143/jjap.51.070203>
- Atilgan, A., Yildiz, A., Harmanci, U.:  $\beta$ -Ga O nanoflakes/p-si heterojunction self-powered photodiodes. *Mater. Today Commun.* **24**, 101105 (2020). <https://doi.org/10.1016/j.mtcomm.2020.101105>
- Bai, Z., Zhang, Y.: Self-powered UV–visible photodetectors based on ZnO/Cu<sub>2</sub>O nanowire/electrolyte heterojunctions. *J. Alloys Compd.* **675**, 325–330 (2016). <https://doi.org/10.1016/j.jallcom.2016.03.051>
- Chan, D.Y.C., Mitchell, D.J., Ninham, B.W.: Short-range interactions mediated by a solvent with surface adhesion. *Mol. Phys.* **35**(6), 1669–1679 (1978). <https://doi.org/10.1080/0026897780010251>
- Chen, X., Liu, K., Zhang, Z.: Self-powered solar-blind photodetector with fast response based on Au/ $\beta$ -Ga<sub>2</sub>O<sub>3</sub> nanowires array film Schottky junction. *ACS Appl. Mater. Inter.* **8**(6), 4185–4191 (2016). <https://doi.org/10.1021/acsaami.5b11956>
- Chen, K., Wang, S., He, C.: Photoelectrochemical self-powered solar-blind photodetectors based on Ga<sub>2</sub>O<sub>3</sub> nanorod array/electrolyte solid/liquid heterojunctions with a large separation interface of photogenerated carriers. *ACS Appl. Nano Mater.* **2**(10), 6169–6177 (2019). <https://doi.org/10.1021/acsaanm.9b00992>
- Chen, Y., Wang, Y., Wang, Z.: Unipolar barrier photodetectors based on van der Waals heterostructures. *Nat. Electron.* **4**(5), 357–363 (2021). <https://doi.org/10.1038/s41928-021-00586-w>
- Chi, P.-F., Lin, F.-W., Lee, M.-L.: High-responsivity solar-blind photodetectors formed by Ga<sub>2</sub>O<sub>3</sub>/p-GaN bipolar heterojunctions. *ACS Photon.* **9**(3), 1002–1007 (2022). <https://doi.org/10.1021/acsp Photonics.1c01892>
- Cicek, E., McClintock, R., Cho, C.Y.: AlxGa1-xn-based back-illuminated solar-blind photodetectors with external quantum efficiency of 89%. *Appl. Phys. Lett.* **103**(19), 191108 (2013). <https://doi.org/10.1063/1.4829065>
- Fujihara, S., Shibata, Y., Hosono, E.: Chemical deposition of rodlike GaOOH and  $\beta$ -Ga<sub>2</sub>O<sub>3</sub> films using simple aqueous solutions. *J. Electrochem. Soc.* (2005). <https://doi.org/10.1149/1.2060627>
- Fujita, S., Oda, M., Kaneko, K.: Evolution of corundum-structured III-Oxide semiconductors: Growth, properties, and devices. *Jpn. J. Appl. Phys.* (2016). <https://doi.org/10.7567/jjap.55.1202a3>
- Gorokhov, E.V., Magunov, A.N., Feshchenko, V.S.: Solar-blind UV flame detector based on natural diamond. *Instrum. Exp. Technol.* **51**(2), 280–283 (2011). <https://doi.org/10.1134/s002044120802022x>
- Guo, D.Y., Wu, Z.P., An, Y.H.: Oxygen vacancy tuned Ohmic-schottky conversion for enhanced performance in  $\beta$ -Ga<sub>2</sub>O<sub>3</sub> solar-blind ultraviolet photodetectors. *Appl. Phys. Lett.* (2014). <https://doi.org/10.1063/1.4890524>
- Guo, J., Gu, Y., Liu, Y.: Polarization assisted interdigital AlGaIn/GaN heterostructure ultraviolet photodetectors. *IEEE Trans. Electron Devices* **70**(5), 2352–2357 (2023). <https://doi.org/10.1109/ted.2023.3258920>
- He, C., Guo, D., Chen, K.:  $\alpha$ -Ga<sub>2</sub>O<sub>3</sub> nanorod array-Cu<sub>2</sub>O microsphere p–n junctions for self-powered spectrum-distinguishable photodetectors. *ACS Appl. Nano Mater.* **2**(7), 4095–4103 (2019). <https://doi.org/10.1021/acsaanm.9b00527>
- He, T., Ma, H., Wang, Z.: On-chip optoelectronic logic gates operating in the telecom band. *Nat. Photonics* **18**(1), 60–67 (2023). <https://doi.org/10.1038/s41566-023-01309-7>
- Hou, Y.N., Mei, Z.X., Liang, H.L.: Dual-band MgZnO ultraviolet photodetector integrated with si. *Appl. Phys. Lett.* (2013). <https://doi.org/10.1063/1.4802486>

- Hu, W.D., Chen, X.S., Ye, Z.H., Lu, W.: A hybrid surface passivation on HgCdTe long wave infrared detector with in-situ CdTe deposition and high-density hydrogen plasma modification. *Appl. Phys. Lett.* **99**(9), 091101 (2011). <https://doi.org/10.1063/1.3633103>
- Hu, W., Ye, Z., Liao, L.: 128×128 long-wavelength/mid-wavelength two-color HgCdTe infrared focal plane array detector with ultralow spectral cross talk. *Opt. Lett.* **39**(17), 5184–5187 (2014). <https://doi.org/10.1364/ol.39.005184>
- Huang, L., Hu, Z., Zhang, H.: A simple, repeatable and highly stable self-powered solar-blind photoelectrochemical-type photodetector using amorphous Ga<sub>2</sub>O<sub>3</sub> films grown on 3D carbon fiber paper. *J. Mater. Chem. C* **9**(32), 10354–10360 (2021a). <https://doi.org/10.1039/d1tc02471j>
- Huang, L., Hu, Z., He, X.: Self-powered solar-blind ultraviolet photodetector based on  $\alpha$ -Ga<sub>2</sub>O<sub>3</sub> nanorod arrays fabricated by the water bath method. *Opt. Mater. Express* (2021b). <https://doi.org/10.1364/ome.431377>
- Khranovskyy, V., Ekblad, T., Yakimova, R., Hultman, L.: Surface morphology effects on the light-controlled wettability of ZnO nanostructures. *Appl. Surf. Sci.* **258**(20), 8146–8152 (2012). <https://doi.org/10.1016/j.apusc.2012.05.011>
- Kokkoli, E., Zukoski, C.F.: Effect of solvents on interactions between hydrophobic self-assembled monolayers. *J. Colloid Interface Sci.* **209**, 60–65 (1999)
- Kong, W.Y., Wu, G.A., Wang, K.Y.: Graphene-beta-Ga<sub>2</sub>O<sub>3</sub> heterojunction for highly sensitive deep UV photodetector application. *Adv. Mater.* **28**(48), 10725–10731 (2016). <https://doi.org/10.1002/adma.201604049>
- Lan, Y.-P.: The influence of the preheating temperature of the (-201)  $\beta$ -Ga<sub>2</sub>O<sub>3</sub> substrates on c-plane GaN epitaxial growth. *Coatings* (2021). <https://doi.org/10.3390/coatings11070824>
- Lewis, B.: The growth of crystals of low supersaturation. *J. Cryst. Growth* **21**, 29–39 (1974)
- Li, Q., Wei, L., Xie, Y.: ZnO nanoneedle/H<sub>2</sub>O solid-liquid heterojunction-based self-powered ultraviolet detector. *Nanoscale Res. Lett.* **8**, 415 (2013)
- Li, H., Jiao, S., Li, H.: Tunable growth of PbS quantum Dot-ZnO heterostructure and mechanism analysis. *Cryst. Eng. Commun.* **17**, 4722–4728 (2015)
- Li, S., Guo, D., Li, P.: Ultrasensitive, super high signal-to-noise ratio, self-powered solar-blind photodetector based on n-Ga<sub>2</sub>O<sub>3</sub>/p-CuSCN core-shell microwire heterojunction. *ACS Appl. Mater. Interfaces* **11**(38), 35105–35114 (2019). <https://doi.org/10.1021/acsami.9b11012>
- Liang, H., Meng, F., Lamb, B.K.: Solution growth of screw dislocation driven  $\alpha$ -GaOOH nanorod arrays and their conversion to porous ZnGa<sub>2</sub>O<sub>4</sub> nanotubes. *Chem. Mater.* **29**(17), 7278–7287 (2017). <https://doi.org/10.1021/acs.chemmater.7b01930>
- Liao, M., Wang, X., Teraji, T.: Light intensity dependence of photocurrent gain in single-crystal diamond detectors. *Phys. Rev. B* (2010). <https://doi.org/10.1103/PhysRevB.81.033304>
- Lin, H., Wei, L., Wu, C.: High-performance self-powered photodetectors based on ZnO/ZnS core-shell nanorod arrays. *Nanoscale Res. Lett.* **11**(1), 420 (2016). <https://doi.org/10.1186/s11671-016-1639-7>
- Mahmoud, W.E.: Solar blind avalanche photodetector based on the cation exchange growth of  $\beta$ -Ga<sub>2</sub>O<sub>3</sub>/SnO<sub>2</sub> bilayer heterostructure thin film. *Sol. Energ. Mater. Sol. C.* **152**, 65–72 (2016). <https://doi.org/10.1016/j.solmat.2016.03.015>
- Morkoç, H., Strite, S., Gao, G.B.: Large-band-gap SiC, III–V nitride, and II–VI ZnSe-based semiconductor device technologies. *J. Appl. Phys.* **76**(3), 1363–1398 (1994). <https://doi.org/10.1063/1.358463>
- Ni, D., Wang, Y., Li, A.: Ald oxygen vacancy-rich amorphous Ga<sub>2</sub>O<sub>3</sub> on three-dimensional urchin-like ZnO arrays for high-performance self-powered solar-blind photodetectors. *Nanoscale* **14**(8), 3159–3165 (2022). <https://doi.org/10.1039/d1nr08262k>
- Onuma, T., Saito, S., Sasaki, K.: Valence band ordering in  $\beta$ -Ga<sub>2</sub>O<sub>3</sub> studied by polarized transmittance and reflectance spectroscopy. *Jpn. J. Appl. Phys.* (2015). <https://doi.org/10.7567/jjap.54.112601>
- Orita, M., Ohta, H., Hirano, M.: Deep-ultraviolet transparent conductive  $\beta$ -Ga<sub>2</sub>O<sub>3</sub> thin films. *Appl. Phys. Lett.* **77**(25), 4166–4168 (2000). <https://doi.org/10.1063/1.1330559>
- Pearnton, S.J., Yang, J., Cary, P.H.: A review of Ga<sub>2</sub>O<sub>3</sub> materials, processing, and devices. *Appl. Phys. Rev.* **5**(1), 011301 (2018). <https://doi.org/10.1063/1.5006941>
- Qu, L., Ji, J., Liu, X.: Oxygen-vacancy-dependent high-performance Alpha-Ga<sub>2</sub>O<sub>3</sub> nanorods photoelectrochemical deep UV photodetectors. *Nanotechnology* **34**(22), 225203 (2023). <https://doi.org/10.1088/1361-6528/acbfbd>
- Reddy, L.S., Ko, Y.H., Yu, J.S.: Hydrothermal synthesis and photocatalytic property of beta-Ga<sub>2</sub>O<sub>3</sub> nanorods. *Nanoscale Res. Lett.* **10**(1), 364 (2015). <https://doi.org/10.1186/s11671-015-1070-5>
- Tsao, J.Y., Chowdhury, S., Hollis, M.A.: Ultrawide-bandgap semiconductors: research opportunities and challenges. *Adv. Electron. Mater.* **4**(1), 1600501 (2017). <https://doi.org/10.1002/aelm.201600501>

- Wang, Z., Mao, X., Chen, P.: Understanding the roles of oxygen vacancies in hematite-based photoelectrochemical processes. *Angew. Chem. Int. Ed. Engl.* **58**(4), 1030–1034 (2019a). <https://doi.org/10.1002/anie.201810583>
- Wang, S., Chen, K., Zhao, H.: Beta-Ga<sub>2</sub>O<sub>3</sub> nanorod arrays with high light-to-electron conversion for solar-blind deep ultraviolet photodetection. *RSC Adv.* **9**(11), 6064–6069 (2019b). <https://doi.org/10.1039/c8ra10371b>
- Wang, Y., Wu, C., Guo, D.: All-Oxide NiO/Ga<sub>2</sub>O<sub>3</sub> p–n junction for self-powered uv photodetector. *ACS Appl. Electron. Mater.* **2**(7), 2032–2038 (2020a). <https://doi.org/10.1021/acsaelm.0c00301>
- Wang, Y., Shi, X., Oshikiri, T.: Plasmon-induced electron injection into the large negative potential conduction band of Ga<sub>2</sub>O<sub>3</sub> for coupling with water oxidation. *Nanoscale* **12**(44), 22674–22679 (2020b). <https://doi.org/10.1039/d0nr06319c>
- Wang, G., Bai, Z., Wu, H.: A wire-shaped and high-sensitivity photoelectrochemical ultraviolet photodetector based on TiO<sub>2</sub> nanotube arrays. *Appl. Phys. Lett.* (2022). <https://doi.org/10.1063/5.0102834>
- Wang, G., Zhang, X., Li, J.: A wire-shaped photoanode of the solar-blind photoelectrochemical-type photodetector based on an  $\alpha$ -Ga<sub>2</sub>O<sub>3</sub> nanorods/electrolyte solid/liquid heterojunction. *Appl. Phys. Lett.* (2023). <https://doi.org/10.1063/5.0134093>
- Wu, Z., Jiao, L., Wang, X.: A self-powered deep-ultraviolet photodetector based on an epitaxial Ga<sub>2</sub>O<sub>3</sub>/Ga:ZnO heterojunction. *J. Mater. Chem. C* **5**(34), 8688–8693 (2017). <https://doi.org/10.1039/c7tc01741c>
- Wu, C., Qiu, L., Li, S.: High sensitive and stable self-powered solar-blind photodetector based on solution-processed all inorganic CuMoO<sub>2</sub>/Ga<sub>2</sub>O<sub>3</sub> pn heterojunction. *Mat. Today Phys.* **17**, 100335 (2021). <https://doi.org/10.1016/j.mtphys.2020.100335>
- Yan, Z., Li, S., Liu, Z.: High sensitivity and fast response self-powered solar-blind ultraviolet photodetector with a  $\beta$ -Ga<sub>2</sub>O<sub>3</sub>/spiro-MeOTAD p–n heterojunction. *J. Mater. Chem. C* **8**(13), 4502–4509 (2020). <https://doi.org/10.1039/c9tc06767a>
- You, D., Xu, C., Zhao, J.: Vertically aligned ZnO/Ga<sub>2</sub>O<sub>3</sub> core/shell nanowire arrays as self-driven superior sensitivity solar-blind photodetectors. *J. Mater. Chem. C* **7**(10), 3056–3063 (2019). <https://doi.org/10.1039/c9tc00134d>
- Zhang, D., Zheng, W., Lin, R.: Ultrahigh EQE (15%) solar-blind uv photovoltaic detector with organic–inorganic heterojunction via dual built-in fields enhanced photogenerated carrier separation efficiency mechanism. *Adv. Funct. Mater.* (2019a). <https://doi.org/10.1002/adfm.201900935>
- Zhang, J., Jiao, S., Wang, D.: Solar-blind ultraviolet photodetection of an  $\alpha$ -Ga<sub>2</sub>O<sub>3</sub> nanorod array based on photoelectrochemical self-powered detectors with a simple, newly-designed structure. *J. Mater. Chem. C* **7**(23), 6867–6871 (2019b). <https://doi.org/10.1039/c9tc01417a>
- Zhang, J., Jiao, S., Wang, D.: Nano tree-like branched structure with  $\alpha$ -Ga<sub>2</sub>O<sub>3</sub> covered by  $\gamma$ -Al<sub>2</sub>O<sub>3</sub> for highly efficient detection of solar–blind ultraviolet light using self-powered photoelectrochemical method. *Appl. Surf. Sci.* (2021). <https://doi.org/10.1016/j.apsusc.2020.148380>
- Zhang, B., Wu, H., Feng, C.: Self-powered solar-blind photodetectors based on  $\alpha$ -Ga<sub>2</sub>O<sub>3</sub> nanorod arrays. *ACS Appl. Nano Mater.* **5**(8), 11956–11963 (2022a). <https://doi.org/10.1021/acsnm.2c03015>
- Zhang, C., Liu, K., Ai, Q.: Performance enhancement of Ga<sub>2</sub>O<sub>3</sub> solar-blind UV photodetector by the combination of oxygen annealing and plasma treatment. *J. Phys. Chem. C* **126**(51), 21839–21846 (2022b). <https://doi.org/10.1021/acs.jpcc.2c07141>
- Zhang, J., Jiao, S., Wan, Y.: A well-grown  $\beta$ -Ga<sub>2</sub>O<sub>3</sub> microrod array formed from GaOOH on a Si (100) substrate and growth mechanism study. *Cryst. Eng. Comm.* **20**(30), 4329–4335 (2018). <https://doi.org/10.1039/c8ce00658j>
- Zhuo, R., Wu, D., Wang, Y.: A self-powered solar-blind photodetector based on a MoS<sub>2</sub>/ $\beta$ -Ga<sub>2</sub>O<sub>3</sub> heterojunction. *J. Mater. Chem. C* **6**(41), 10982–10986 (2018). <https://doi.org/10.1039/c8tc04258f>

**Publisher's Note** Springer Nature remains neutral with regard to jurisdictional claims in published maps and institutional affiliations.

Springer Nature or its licensor (e.g. a society or other partner) holds exclusive rights to this article under a publishing agreement with the author(s) or other rightsholder(s); author self-archiving of the accepted manuscript version of this article is solely governed by the terms of such publishing agreement and applicable law.